# An FTIR study of the electrooxidation of C2 and C3 alcohols on carbon-supported PdxRhy in alkaline medium

Thamyres Moreira, Adalgisa Andrade, K. Boniface Kokoh, Cláudia Morais, Teko Napporn, Paulo Olivi

# An FTIR study of the electrooxidation of C2 and C3 alcohols on carbon-supported PdxRhy in alkaline medium

Thamyres F. M. Moreira[a,b], Adalgisa R. Andrade[a], K. Boniface Kokoh[b], Cláudia Morais[b], Teko W. Napporn[b]*, Paulo Olivi*[a]

[a] Dr. Thamyres F. M. Moreira, Prof. Dr. Adalgisa R. Andrade, Prof. Dr.Paulo Olivi*
Departamento de Química
Faculdade de Filosofia, Ciências e Letras de Ribeirão Preto
Universidade de São Paulo Ribeirão Preto 14040-901, Brazil.
E-mail: olivip@usp.br

[b] Dr. Thamyres F. M. Moreira, Prof. Dr. Kouakou Boniface Kokoh, Dr. Cláudia Morais, Dr. Teko W. Napporn
Department of Chemistry
IC2MP CNRS UMR 7285, Université de Poitiers
4 rue Michel Brunet - B27, TSA 51106, 86073 Cedex 9 (France).
E-mail: teko.napporn@univ-poitiers.fr

Supporting information for this article is given via a link at the end of the document

**Abstract:** We have investigated the promoting effect of Rh addition to Pd-based materials in the electrooxidation of ethanol and glycerol. Physicochemical characterizations (XRD, EDX, TEM, and XPS) of the PdxRhy/C materials, prepared by Bromide Anion Exchange (BAE), showed that the experimental bimetallic compositions were close to the targeted ones. PdxRhy/C particle sizes ranged from 2.2 to 3.8 nm. The ethanol oxidation reaction (EOR) on the PdxRhy/C catalysts yielded four times larger carbonate ($CO_3^{2-}$) amount. As for the glycerol oxidation reaction (GOR), the onset potential on the $Pd_{50}Rh_{50}$/C catalyst occurred at lower potentials. Chromatographic analysis combined with *in situ* Fourier transform infrared (FTIR) spectroscopy showed that GOR on the $Pd_{50}Rh_{50}$/C catalyst selectively and quantitatively produced glycerate and tartronate. The outstanding ability of the $Pd_{50}Rh_{50}$/C catalyst toward EOR and GOR was correlated to the electronic effect expressed by a negative potential shift (200 mV) and the 47% alloying degree in the $Pd_{50}Rh_{50}$/C structure.

## Introduction

Direct alcohol fuel cells (DAFCs) are an attractive and promising technology for transportation and portable electronic devices that run on fuels obtained from biomass valorization [1, 2]. Ethanol ($C_2$) and glycerol ($C_3$) are advantageous organic molecules in terms of energy density, distribution, fuel cost, and lower toxicity [3, 4]. Ethanol is an attractive fuel: it can be obtained from renewable sources and presents low toxicity and high-energy density (8 kWh $kg^{-1}$) [5, 6]. Glycerol is a byproduct of biodiesel production and is a valuable feedstock for fuel cell devices because it allows energy to be generated and value-added products to be electrosynthesized [7-14]. Although DAFCs are environmentally friendly and present sustainable characteristics, these energy devices have slower reaction kinetics at the low temperature of cell operation [1, 15]. For alcohols bearing more than two carbons, complete oxidation to $CO_2$ (or carbonate) is limited by C–C bond cleavage. In addition, formation of species such as carbon monoxide (CO) diminishes oxidation efficiency [3, 16, 17]. Therefore, designing more selective and effective catalyst materials for DAFCs is crucial to this technology.

In alkaline medium, palladium-based catalysts are an interesting alternative to platinum-based catalysts when it comes to catalytic properties [18, 19]. When the Pd electrode is used as a mono-metal electrode in alkaline medium, its catalytic properties resemble or are even better than the catalytic properties of the Pt electrode [4]. The electrocatalytic performance of Pd improves in the presence of a co-catalyst: Pd activity and durability increase considerably due to the synergistic effect arising from the electronic effect of the added metal on the Pd *d*-band center, to the resulting bifunctional catalyst, or to both [4, 19-26].

When rhodium is added to Pt-based catalysts, it promotes C-C bond cleavage in the Ethanol Oxidation Reaction (EOR) [27-30] and Glycerol Oxidation Reaction (GOR) at low potentials [8]. Nevertheless, there are few reports on the beneficial effects of Rh addition to Pd-based catalysts for alcohol oxidation. Ferreira Jr *et al*. [10] investigated GOR on a non-supported $Pd_{70}Rh_{30}$ catalyst by *in situ* FTIRS in alkaline medium. They concluded that carbonate ($CO_3^{2-}$) was the main product of glycerol electrooxidation, and that Rh favored C-C bond cleavage at low potentials. However, the authors did not evaluate the physicochemical characterization data. Recently, Fontes and co-workers [31] studied the activity of a PdRh catalyst on EOR in alkaline medium and demonstrated how Rh addition affected product distribution by *in situ* FTIR analyses. These authors found that acetate and carbonate ions emerged along all the applied potential range, at larger amounts than those obtained for Pd catalysts, which indicated the presence of an associative character regarding ethanol adsorption on the PdRh catalyst. Maksić *et al.* [32] studied how Rh deposited onto polycrystalline Pd impacted EOR in alkaline medium. They noticed that Rh addition to the Pd catalyst accelerated the reaction *via* an electronic effect. Nevertheless, more contributions are necessary to understand the effects of Rh addition.

Improvement in catalytic properties is also related to the synthesis process [15, 24, 33-36]. In terms of applicability, using clean, simple, low-cost, and lowly toxic methods to prepare catalysts is essential [37]. In this context, our research group developed the bromide anion exchange (BAE) method. In BAE, chloride ions are replaced with bromide ions in the complex structure of the metal cation, followed by a reduction process [12, 37, 38]. This provides more efficient particle growth because bromide has larger atomic radius than chloride. Compared to other synthesis methods, like the borohydride reduction method [16, 39-41], BAE allows nanoparticle size and shape to be controlled, which reflects directly on the activity of the catalyst material. The use of BAE to obtain Pd-based catalysts has enabled catalysts containing gold [37], silver [12], iron [38], manganese [38], and nickel [42, 43] to be prepared. There are no studies on Rh-containing catalysts obtained by this synthesis protocol. In this scenario, we aim to evaluate how Rh addition to Pd catalysts influences catalyst structure,

electrooxidation performance, and reaction product distribution. We will identify the products and intermediates from EOR and GOR by high-performance liquid chromatography (HPLC) coupled with ultraviolet-visible (UV-VIS) detector followed by refractive index detector (RID) (HPLC-UV/RID), and by *in situ* Fourier transform infrared (FTIR) spectroscopy.

## Results and Discussion

*Physicochemical characterization*

We characterized the $Pd_xRh_y$/C nanocatalysts to determine their effective metal loading, crystallographic structure, and elemental and surface composition. **Figure S1** shows the representative thermogravimetric analysis. The metal loadings were close to the target theoretical values (20 %) (**Table 1**). **Figure S2a** depicts the XRD patterns of the $Pd_xRh_y$/C nanocatalysts. All the samples displayed a peak at 2θ = 25°, assigned to the (002) reflection plane of carbon Vulcan, used as substrate. Compared to the diffractograms of the Pd/C and Rh/C catalysts, the diffractograms of the $Pd_xRh_y$/C catalysts presented the Pd face-centered cubic (*fcc*) profile with the main facets (111), (200), and (220). The crystallite size (*Lv*), determined with the Scherrer equation by using the reflection plane (111) [44], decreased in the bimetallic compositions and tended toward *Lv* of Rh as the Rh content increased (**Table 1**). The crystallite sizes obtained by BAE were satisfactory for EOR and GOR applications. For example, Fontes et al. [31] prepared $Pd_{50}Rh_{50}$ by the borohydride reduction method and obtained particle size close to 10 nm, while herein the same composition had particle size of 2.4 nm. Additionally, a decrease in particle size increases the active surface, thereby increasing the catalytic activity. **Figure S2a** depicts a positive shift in the 2θ values that matches with the increase in the Rh amount in the bimetallic compositions, suggesting that an alloy between Pd and Rh was formed during the synthesis. To confirm this effect, we estimated the crystal lattice parameter ($a_{hkl}$) of each catalyst as described previously [11, 45]. **Figure S2b** shows the relation between the lattice parameter and the Rh content in the catalysts. Above 20% Rh content, the lattice parameter values decreased linearly, indicating alloy formation according to the Vegard's law (**Table 1**). The $Pd_{50}Rh_{50}$/C catalyst had the highest alloying degree, 47%. Moreover, the Pd/C and Rh/C catalysts presented experimental lattice parameters of 0.3817 and 0.3801 nm, respectively, which were very close to the theoretical values 0.3890 nm for Pd and 0.3803 nm for Rh [27, 46]. We also determined the atomic ratio in the $Pd_xRh_y$/C catalysts by EDX analysis. **Table 1** shows that the experimental compositions were very close to the theoretical ones.

**Table 1.** Physicochemical parameters determined for the PdxRhy/C catalysts.

| Catalyst | Experimental Composition (EDX %) | 2θ theta (degrees) | Crystallite size (nm) (XRD) | Lattice parameter (nm) | Alloying Degree (%) |
|---|---|---|---|---|---|
| **Pd/C** | --- | 39.824 | 3.6 | 0.3917 | --- |
| **Rh/C** | --- | 41.109 | 2.2 | 0.3800 | --- |
| **$Pd_{50}Rh_{50}$/C** | $Pd_{54}Rh_{46}$ | 40.269 | 2.4 | 0.3876 | 47 |
| **$Pd_{60}Rh_{40}$/C** | $Pd_{62}Rh_{38}$ | 40.121 | 2.2 | 0.3889 | 34 |
| **$Pd_{70}Rh_{30}$/C** | $Pd_{70}Rh_{30}$ | 39.973 | 3.8 | 0.3903 | 23 |
| **$Pd_{80}Rh_{20}$/C** | $Pd_{78}Rh_{22}$ | 39.824 | 3.6 | 0.3917 | -- |

Electrocatalytic reactions, such as those considered in this work, are surface reactions [24, 47, 48]. This requires that the surface layer of each prepared catalyst is examined to gain insight into the surface composition that will be in contact with the organic molecules under investigation. Accordingly, we resorted to XPS measurements to characterize the surface layers of the prepared catalysts. We took the $Pd_{50}Rh_{50}$/C catalyst as example to determine impurities and performed fine deconvolution analyses on the 3d bands of Pd and Rh in the bimetallic material. **Figure S3** illustrates the XPS spectra of Pd3d and Rh3d fittings to the surface chemical composition, and **Table 2** lists the intensities of the XPS peaks for the oxidation states of the constituents. Analysis of the surface chemical composition revealed the presence of oxides of both metals. Oxides can interact favorably to activate the catalyst material by oxidative removal of the reaction intermediates (L-H mechanism or bifunctional catalysis) [49].

**Table 2.** Experimental data from the XPS spectra fitting related to analysis of the $Pd_{50}Rh_{50}$/C catalyst.

| Binding Energy / eV | Corresponding Band | Species | Relative atomic percentage / % | Binding Energy / eV |
|---|---|---|---|---|
| 335.4 | Pd 3d | Pd metallic | 0.3 | 335.4 |
| 336.9 | | $Pd^{2+}$ (PdO) | 1.3 | 336.9 |
| 348.3 | | Pd oxide ($PdO_2$) | 0.4 | 348.3 |
| 307.2 | Rh 3d | Rh metallic | 0.4 | 307.2 |
| 308.4 | | $Rh^{3+}$ ($Rh_2O_3$) | 1 | 308.4 |

*Electrochemical Characterization of PdxRhy/C catalysts*

To evaluate how Rh affected the catalytic behavior of the Pd-based catalysts, we conducted a series of electrochemical measurements, which consisted of characterizing each catalyst by cyclic voltammetry, assessing their electrocatalytic activity through a probe molecule (CO-stripping), or coupling electrochemical polarization to the *in situ* infrared spectroscopy technique.

*CO-stripping experiments coupled with FTIR spectroscopy*

CO-stripping is an electrochemical method for probing the activity of a catalyst when an organic fuel such as ethanol or glycerol is studied. Indeed, CO is the poisoning species at the anode during fuel oxidation [1], so this type of characterization allows the ability of the $Pd_xRh_y$/C catalysts to resist active site poisoning by CO to be evaluated in real time. **Figure 1a** depicts representative cyclic voltammograms of the prepared catalysts in 0.10 mol $L^{-1}$ NaOH, as supporting electrolyte. All the current densities were normalized with the metal loading on the conducting substrate. The Pd/C and Rh/C catalysts exhibited the typical voltammograms of Pd and Rh nanoparticles supported on carbon, recorded in an alkaline medium [31]. For the bimetallic catalysts, Rh clearly influenced the CV profile. The hydrogen adsorption/desorption region expanded as the Rh content increased. **Figure 1b** displays the first forward linear scan during the CO stripping experiment at 10 mV $s^{-1}$. The CO-to-carbonate

oxidation strongly depended on the catalyst composition. More importantly, the CO oxidation peak shifted toward lower potentials as the Rh content increased. The shift was as high as 300 mV for CO oxidation on the Pd/C catalyst as compared to the $Pd_{50}Rh_{50}$/C catalyst.

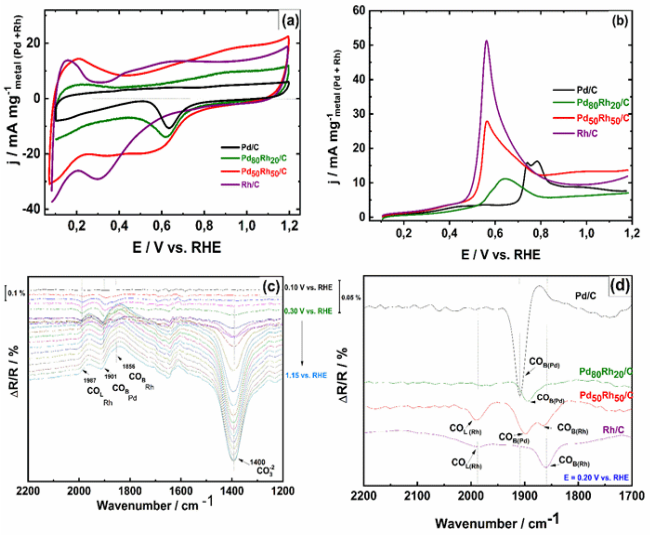


**Figure 1.** **(a)** Voltammograms of the $Pd_xRh_y$/C catalysts at 10 mV $s^{-1}$; **(b)** CO stripping on the Pd-based catalysts at 10 mV $s^{-1}$; **(c)** SPAIR spectra recorded during CO stripping measurement on the $Pd_{50}Rh_{50}$/C catalyst. Reference spectrum taken at 0.10 V *vs* RHE; **(d)** FTIR spectra obtained during CO stripping at 0.20 V vs RHE on the Pd/C, Rh/C, $Pd_{80}Rh_{20}$/C, and $Pd_{50}Rh_{50}$/C catalysts. Supporting electrolyte is 0.10 mol $L^{-1}$ NaOH at room temperature.

**Figure 1c** shows the IR spectra of CO vibrations at the surface of the reference catalyst ($Pd_{50}Rh_{50}$/C). When the potential varied from 0.1 to 1.15 V *vs* RHE at low scan rate (1 mV $s^{-1}$), it was possible to notice the different modes of CO adsorption at the active sites of Rh and Pd. Indeed, the CO-to-$CO_3^{2-}$ oxidation (band at 1392 $cm^{-1}$) occurred through linear adsorption ($CO_L$) on Rh (band at 1987 $cm^{-1}$) and through bridged-bond CO ($CO_B$) on Pd (band at 1909 $cm^{-1}$) and Rh (band at 1863 $cm^{-1}$) [50].
**Figure 1d** shows that the presence of Rh completely modified CO adsorption on the $Pd_{80}Rh_{20}$/C and $Pd_{50}Rh_{50}$/C catalysts as compared to CO adsorption on the Pd/C catalyst (**Figure S4**). Increasing Rh content decreased the intensity of the bands due to CO adsorption, which were divided into two modes ($CO_B$ on Pd, $CO_B$ on Rh, and $CO_L$ on Rh) instead of $CO_B$ alone on the Pd/C catalyst. Increasing Rh content also shifted the band due to $CO_B$ in the Pd/C catalyst from 1909 to 1896 $cm^{-1}$, with an additional band arising at 1863 $cm^{-1}$ for $CO_B$ on Rh, as though the trend toward low wavenumbers is strongly related to earlier oxidative removal. As a result, the behavior of the probe molecule CO at the $Pd_{50}Rh_{50}$/C surface highlighted the effect of Rh binding to Pd during alloy formation, which weakened the Rh-$CO_{ads}$ interaction for CO oxidation at lower potentials [51-56].

*Ethanol Oxidation Reaction (EOR) on $Pd_xRh_y$/C catalysts*

**Figure 2a** shows the EOR polarization curves on the $Pd_xRh_y$/C catalysts. First, Rh addition to the Pd/C catalyst raised the current densities considerably. The EOR at low Rh content improved the structural effect on the anode material, increasing the current densities[49]. When the Rh content reached 50%, not only did the oxidation peak increase (two-fold at 0.7 V *vs* RHE), but the aforementioned ligand effect improved the catalyst, shifting the ethanol oxidation peak to 0.14 V *vs* RHE compared to 0.35 V *vs* RHE for the Pd/C catalyst.

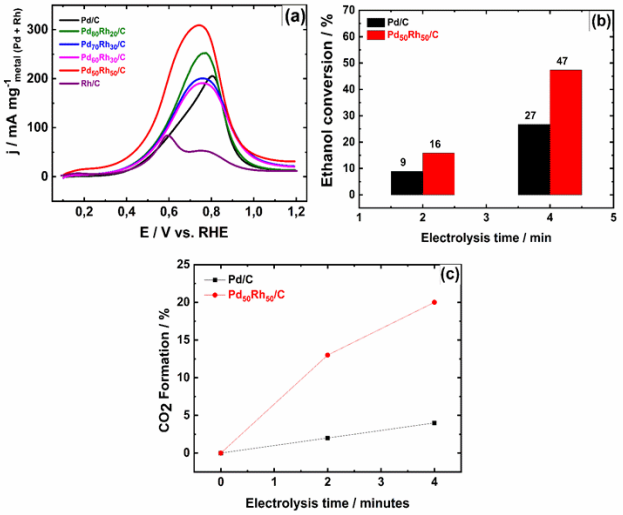


**Figure 2.** **(a)** Cyclic voltammograms of the $Pd_xRh_y$/C catalysts recorded in 0.10 mol $L^{-1}$ NaOH in the presence of 0.2 mol $L^{-1}$ ethanol at room temperature and 10 mV $s^{-1}$; **(b)** Ethanol conversion on the Pd/C and $Pd_{50}Rh_{50}$/C catalysts after electrolysis for 2 and 4 hours at 0.60 V *vs* RHE; **(c)** Carbon dioxide (or $CO_3^{2-}$) formation on the Pd/C and $Pd_{50}Rh_{50}$/C catalysts as a function of electrolysis time.

Several studies have shown that EOR is incomplete when an average of four electrons are involved instead of the 12 electrons that are needed for total ethanol oxidation to $CO_2$ [16, 27, 57-61]. Incomplete EOR is due to the ethanol structure, which is composed of two carbons that do not have the same oxidation states, namely methyl group that is difficult to convert to $CO_2$ and a primary alcohol function that is easy to convert to acetaldehyde and then to acetate [62]. However, Kowal et al.[63, 64] found that the presence of Rh favors C-C bond cleavage, whilst Sn as a co-catalyst promotes acetate production. **Figure 2c** shows that ethanol conversion increased with the residence time in a batch-type electrolysis cell, and that the conversion rate was almost four times higher on $Pt_{50}Rh_{50}$/C than on the Pd/C catalyst. Chromatographic analysis of the electrolytic solution at 0.6 V *vs* RHE revealed that acetate was the predominant product (**Table 3**). The HPLC set-up was equipped with a refractive index detector, which allowed us to use external calibration to determine the concentration of carbonate that was produced (**Figure 2C**). In particular, carbonate appears as a negative peak on the chromatogram because its refractive index is lower than the refractive index of water, which was the solvent. Carbonate ions emerged at fourfold larger amount during oxidation on the $Pd_{50}Rh_{50}$/C catalyst, which meant that the presence of Rh in oxidation states $Rh^{0+}$ and $Rh^{3+}$ (see **Table 2**) promoted and even enhanced dissociative ethanol adsorption and removal of CO-type species as $CO_2$ (or carbonate) from the electrode surface [16, 49].

**Table 3:** Distribution of the reaction products arising from EOR in alkaline electrolyte and on the Pd/C and $Pd_{50}Rh_{50}$/C catalysts.

| Catalyst | Ethanol conversion (%) | Reaction Products | | Mass balance (%) |
|---|---|---|---|---|
| | | Acetate (%) | $CO_3^{2-}$ (%) | |
| **Pd/C** | 27.1 | 83 | 5 | 88 |
| **$Pd_{50}Rh_{50}$/C** | 47.3 | 55 | 20 | 75 |

FTIR spectroscopy is an advanced and powerful *in situ* technique for identifying reaction products and intermediates in real time; *i.e.*, during their adsorption on or at the vicinity of the working electrode. **Figure 3** shows the data obtained for the $Pd_xRh_y/C$ catalysts. The main band assigned to the carbonate ions (1392 $cm^{-1}$) appeared in the same spectral vibration region of acetate, which has three characteristic bands: at 1550, 1410, and 1345 $cm^{-1}$ [8, 65]. Acetate formation was so dominant that the final spectrum resembled the reference spectrum recorded in alkaline medium (**Figure S5**). The only difference was a weak band at 1836 $cm^{-1}$, ascribed to $CO_B$, indicating that the ethanol C-C bond was cleaved (**Figure 3a**). **Figure 3b** illustrates the FTIR spectrum obtained during the chronoamperometric experiment, recorded in the spectroelectrochemical cell under the same conditions of electrolysis; that is, 0.6 V *vs* RHE. Analysis of the data showed that ethanol oxidation on the PdRh/C catalyst produced mainly acetate. Double analysis of the electrolytic solution by HPLC and FTIRS revealed that a small part of ethanol underwent C-C bond cleavage, to form carbonate through oxidation of the $CO_{ads}$ intermediate.

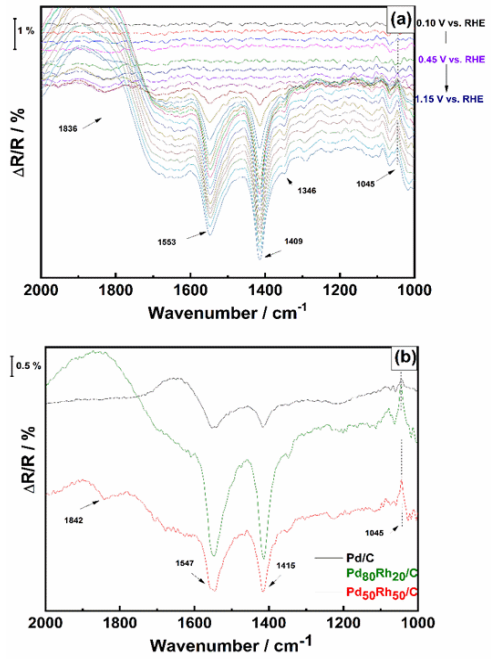


**Figure 3**: (a) SPAIR spectra recorded in 0.1 mol $L^{-1}$ NaOH containing 0.2 mol $L^{-1}$ ethanol at 1 mV $s^{-1}$ on the $Pd_{50}Rh_{50}/C$ catalyst at potentials ranging from 0.10 to 1.20 V *vs* RHE. (b) FTIR spectra recorded during chronoamperometry in 0.1 mol $L^{-1}$ NaOH + 0.2 mol $L^{-1}$ ethanol on the Pd/C, $Pd_{80}Rh_{20}/C$, and $Pd_{50}Rh_{50}/C$ catalysts at 0.6 V *vs* RHE; reaction time = 3 min.

*Glycerol Oxidation Reation (GOR) on $Pd_xRh_y/C$ catalysts*

**Figure 4a** shows the glycerol electrochemical profile during its electrooxidation on the $Pd_xRh_y/C$ catalysts. The glycerol current density peak on the Pd/C catalyst was much higher than on the Rh/C catalyst, but the onset potential for the Rh/C and $Pd_xRh_y/C$ catalysts shifted towards less positive potential. This behavior resembled the behavior observed for EOR. When the Rh content was low (< 40%), the oxidation peak increased, and there was an overlay at the Pd peak position. The $Pd_{50}Rh_{50}/C$ catalyst displayed a large oxidation peak, which suggested that glycerol reacted simultaneously on Rh sites (marked by a shoulder at 0.6 V *vs* RHE) and on Pd sites (peak centered at 0.83 V *vs* RHE).

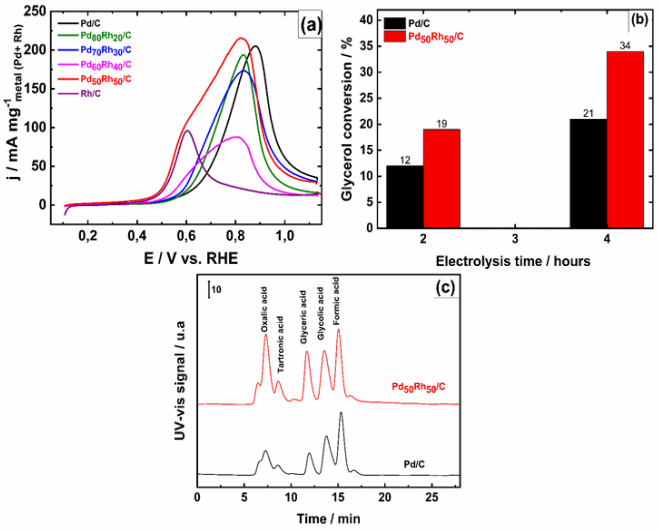


**Figure 4 (a)** Linear scan voltammograms of the $Pd_xRh_y/C$ catalysts recorded in the presence of glycerol at 10 mV $s^{-1}$; **(b)** Glycerol conversion on the Pd/C and $Pd_{50}Rh_{50}/C$ catalysts after electrolysis for 2 and 4 hours at 0.70 V *vs* RHE; **(c)** HPLC after electrolysis for 4 h on the Pd/C and $Pd_{50}Rh_{50}/C$ catalysts. Supporting electrolyte = 0.10 mol $L^{-1}$ NaOH; Gly concentration = 0.2 mol $L^{-1}$

We performed glycerol electrolysis at 0.7 V *vs* RHE on the $Pd_xRh_y/C$ catalysts (**Figure 4b**). Electrocatalytic glycerol conversion was 1.6 times faster on the $Pd_{50}Rh_{50}/C$ catalyst than on the Pd/C catalyst, which facilitated recovery of more reaction products for further chromatographic analyses. **Figure 4c** shows that glycerol was transformed into glycerate and tartronate, and that it underwent C-C bond cleavage to yield oxalate, glycolate, and formate. We did not detect the characteristic carbonate peak in the chromatogram probably because of the low concentration of this ion, the low sensitivity of RID, or both.

Thereafter, we accomplished FTIRS measurements to obtain additional evidence of the reaction products detected by HPLC. For this purpose, we employed two SPAIRS methods: accumulation of interferograms with spectra being recorded every 50 mV (**Figures 5 and S7**) and accumulation of spectra by coupling with a chronoamperometry experiment at 0.55 and 0.70 V *vs* RHE for 30 min (**Figures 5b–d**). Given that the expected products have the same functional groups (carboxyl, hydroxyl...) and that the main bands appear in a very narrow spectral range; we made comparisons with standards recorded in the same electrolytic medium (**Figure S8**). Assignments were established as follows: 1575 $cm^{-1}$ (tartronate), 1363 $cm^{-1}$ (formate), 1420 & 1111 $cm^{-1}$ (glycerate), and 1069 $cm^{-1}$ (glycolate). We attributed the band at 1220 $cm^{-1}$ to glyceraldehyde, according to Holade et al. [43]. This aldehyde is very difficult to determine by HPLC in alkaline medium because it undergoes nucleophilic attack on the carbonyl function, to give glycerate. Electrocatalytic glycerol oxidation also produces $CO_B$ (1902 $cm^{-1}$) and $CO_2$ (2340–2345 $cm^{-1}$) (**Figure 5**). Although we carried out the reaction in basic solution, the appearance of the $CO_2$ band could be explained by the acidity of local pH; i.e., the pH in the vicinity of the electrode confined in an electrolytic film, which allowed time for $CO_2$ to diffuse into the bulk to be transformed into carbonate.

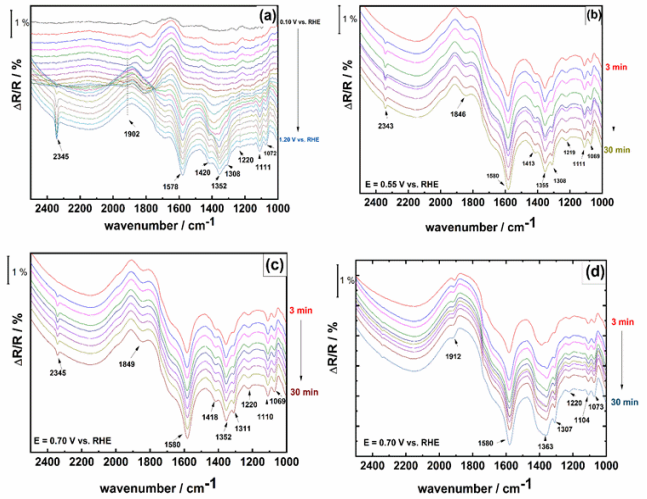


**Figure 5: (a)** SPAIRS spectra recorded in 0.1 mol $L^{-1}$ NaOH containing 0.1 mol $L^{-1}$ glycerol at 1 mV $s^{-1}$ on the $Pd_{50}Rh_{50}$/C catalyst; **(b)** FTIR spectra recorded during chronoamperometry experiment on the $Pd_{50}Rh_{50}$/C catalyst at 0.55 V *vs* RHE; **(c)** FTIR spectra recorded during chronoamperometry experiment on the $Pd_{50}Rh_{50}$/C catalyst at 0.70 V *vs* RHE; **(d)** FTIR spectra recorded during chronoamperometry experiment on the Pd/C catalyst 0.70 V *vs* RHE.

## Conclusion

We have successfully prepared $Pd_xRh_y$/C catalysts by the BAE method and used them as anodes during ethanol and glycerol electrooxidation. We have correlated a series of electrochemical measurements coupled with spectroelectrochemistry (FTIRS) to physicochemical characterizations to understand and to interpret the reaction pathways of ethanol and glycerol oxidation on the $Pd_xRh_y$/C nanocatalysts. Taking the $Pd_{50}Rh_{50}$/C catalyst as the reference anode for these investigations, the CO-stripping/SPAIRS experiments showed that this probe molecule adsorbs on Pd in a bridged form. When Rh is added to Pd, CO adsorption takes place under three modes ($CO_B$ on Rh and Pd sites, and $CO_L$ on Rh). The XRD and XPS characterizations revealed that the alloying degree reaches 47% in the $Pd_{50}Rh_{50}$/C catalyst, which provides Pd with a beneficial ligand effect that helps to deplete the poisoning CO species strongly adsorbed on the catalyst surface. On the other hand, in the bimetallic catalysts, Rh is available in three oxidation states – $Rh^0$ and $Rh^{3+}$ – which are known to participate in C-C bond cleavage and to promote transformation of $CO_{ads}$ into $CO_2$ (or carbonate in alkaline medium). Chromatographic analyses undertaken to determine the ethanol conversion products indicated that, apart from acetate as the main product, the carbonate concentration is four times higher in the presence of the $Pd_{50}Rh_{50}$/C catalyst compared to the Pd/C catalyst. In the case of glycerol, its selective oxidation allows valorization of this molecule, which results from the synthesis of biodiesel into value-added chemicals. Thus, electrochemical studies performed and coupled with analytical and spectroscopic methods revealed that electrocatalytic glycerol oxidation on the $Pd_{50}Rh_{50}$/C catalyst affords tartronate and glycerate. Additionally, we identified C-C bond cleavage products (oxalate, glycolate, formate, and carbonate).

## Experimental Section

*Chemicals*

Potassium tetrachloropalladate ($K_2PdCl_4$, 99%), rhodium (III) chloride hydrate ($RhCl_3.xH_2O$ Rh basis $\geq$ 38 %), sodium borohydride ($NaBH_4$, 99%), and potassium bromide (KBr, 99%) were purchased from Sigma-Aldrich and used as received during the synthesis of the $Pd_xRh_y$/C catalysts. To prepare well-dispersed nanoparticles supported on a conducting substrate, Vulcan carbon XC 72R from Cabot was added to the synthesis solution. Two alcohols were investigated as potential fuels, ethanol ($C_2H_6O$, 99%) and glycerol (ReagentPlus > 99%), which were acquired from Merck and Sigma-Aldrich, respectively. Standards of all the molecules that were likely to be formed during EOR or GOR; *i.e*. acetic, tartronic, glyceric, glycolic, glyoxylic, oxalic acid, and formic acids, as well as sodium carbonate were supplied by Sigma-Aldrich and employed for HPLC internal calibration. All the solutions were prepared with Millipore Milli-Q water (18.2 MΩ cm at 20 ºC), and the supporting electrolyte was prepared with sodium hydroxide (NaOH, 97%, from Sigma-Aldrich).

*Catalyst synthesis*

During the BAE synthesis, the metal precursor is reduced in aqueous solution by using bromide ion as capping agent [12, 37]. Bromide has larger ionic radius than chloride, so it forms a more stable and sterically hindered complex, which is advantageous during reduction of the central metal cation. BAE is straightforward to implement, and its optimization consists in controlling the ϕ ratio (or n(KBr)/n(metal (s)), the amount of reducing agent (15-fold excess), and the reaction temperature (40.0 ºC) [12, 37]. Here, different $Pd_xRh_y$/C compositions (x:y atomic ratio = 100:0, 80:20, 70:30, 60:40, 50:50, or 0:100) were prepared by the reaction protocol described as follows. Pd salt, Rh salt, or both were dissolved in 100.0 mL water, and then KBr was added under vigorous stirring for 1 h. After that, carbon Vulcan was added, and the system was kept in an ultrasonic bath for 45 min for the reaction mixture to become thoroughly homogeneous. $NaBH_4$ in cold water was added to the mixture dropwise, and the mixture was stirred at 40 °C for 2 h. Finally, the $Pd_xRh_y$/C catalysts were filtered and exhaustively washed with ultrapure water. The resulting powder was dried at 40 ºC for 24 h. All the catalysts were prepared so that a 20 wt.% metal loading would be achieved [27].

*Physicochemical characterization*

Thermogravimetric analysis (TGA) was used to confirm the metal-loading in the $Pd_xRh_y$/C catalysts and was conducted on a Q600 TA Instruments SDT2960 under synthetic air atmosphere, at a heating rate of 10 °C $min^{-1}$, from 20 to 900 °C. X-ray diffractograms were obtained on an X-ray diffractometer (Bruker - D2 Phaser) with Cu Kα radiation (λ = 0.15406 nm) generated at 30 kV and 10 mA. Diffraction patterns were collected for 2θ values ranging from 20 to 90º, at 0.025º $s^{-1}$. Phase composition was determined by fitting the experimental angular range of interest to the pseudo-Voigt function per crystalline peak with the Profile Plus Executable refinement program (Siemens AG). To estimate crystallite size, the Debye-Scherrer equation was employed. Energy-dispersive X-ray spectroscopy (EDX) was performed on a Leica Zeiss LEO 440 apparatus to check the homogeneity of the local elemental bimetallic compositions of the catalyst materials. X-ray photoelectron spectroscopy (XPS) was used to probe and to characterize the surface and oxidation states of the prepared $Pd_xRh_y$/C nanocatalysts and was accomplished on a Kratos Axis Ultra DLD spectrometer equipped with a monochromatic Al Kα X-ray source operating at 15 kV and 10 mA. The base pressure of the instrument was 9 x $10^{-8}$ Pa. The XPS results are demonstrated by using fitting carried out with the CasaXPS software (version 2.3.17). The internal reference for C1s spectra is centered at 284.6 eV. The Shirley background was chosen, and asymmetric Gaussian-Lorentzian profile functions were used to fit the spectra.

*Electrochemical characterization of catalyst materials*

Electrochemical measurements were performed in a conventional three-electrode cell, on an Autolab Potentiostat (PGSTAT 302N, Metrohm). Hg/HgO/$OH^-$ (0.1 mol $L^{-1}$ NaOH) was used as reference and the counter electrode was a glassy carbon slab. The working electrode was a glassy carbon (GC) disk (3-mm diameter), onto which 5 µL of catalytic ink was uniformly deposited. This ink was prepared by mixing isopropanol (200 µL), water (125 µL), and a Nafion® suspension (30 µL) (5 wt.% in aliphatic alcohols, from Aldrich) and then adding 2.0 mg of the $Pd_xRh_y$/C catalyst powder. The dispersion was homogenized in an ultrasonic bath for 30 min. All the electrolytic solutions were purged with $N_2$ gas for nearly 15 min before any cyclic voltammetry or chronoamperometry measurement. For practical handling and further stability in alkaline environment, Hg/HgO (E = −0.965 V *vs* RHE) was used as reference electrode, but the results were referred to a reversible hydrogen electrode (RHE) for comparison with literature data. Electrocatalytic performance was evaluated by cyclic voltammetry and chronoamperometry at a scan rate of 10 mV $s^{-1}$ in solution containing 0.20 mol $L^{-1}$ ethanol or glycerol. The supporting electrolyte was a 0.10 mol $L^{-1}$ NaOH solution. Cyclic voltammograms were recorded between 0.12 and 1.15 V *vs* RHE. Chronoamperometry tests were conducted at 0.60 V *vs* RHE and 0.70 V *vs* RHE for ethanol and glycerol, respectively, for 30 min. The current densities expressed in the present work were normalized with the total metal loading (Pd + Rh) in the catalyst composition.

*Reaction product analysis and identification*

Reaction products arising from EOR and GOR on the $Pd_xRh_y$ catalysts after electrolysis were characterized and identified by HPLC and *in situ* FTIR spectroscopy. Potentiostatic electrolysis experiments were carried out by setting the electrode potential at 0.60 V and 0.7 V *vs* RHE for ethanol and glycerol, respectively, for 4 h. Every 60 min, a sample of the solution was collected from the anodic compartment for injection into the HPLC apparatus (Shimadzu model LC-10AT), which consisted of a double on-line detection system; *i.e.,* a UV-VIS (λ = 210 nm) detector followed by a refractive index detector (RID-10A). The ion exclusion column (Aminex HPX-87H, from BioRad) was used, and the mobile phase was a diluted sulfuric acid solution (3.33 mmol $L^{-1}$ $H_2SO_4$ at a flow rate of 0.6 mL $min^{-1}$). The automatic injector was equipped with a 20-µL sample loop, which allowed reaction products to be quantitatively determined by external calibration with pure commercial standards injected under the same analytical conditions.
Electrochemical measurements such as CO stripping, cyclic voltammetry, and chronoamperometry were coupled with the SPAIRS (Single Potential Alteration Infrared Reflectance Spectroscopy) technique to monitor the presence of reaction intermediates and the formation of reaction products. Spectra were recorded from 1000 to 4000 $cm^{-1}$; the target region lay between 1000 and 2500 $cm^{-1}$. The spectra were recorded with 8-$cm^{-1}$ spectral resolution and 50-mV intervals between 0.1 and 1.2 V *vs* RHE at a scan rate of 1 mV $s^{-1}$. Reflectance spectra were calculated for the different potential values as changes in the reflectivity ($R_i$) relative to a reference single-beam spectrum ($R_0$), as follows: $\Delta R/R = (R_i - R_0)/R_0$. As already reported [66], simultaneous acquisition of SPAIR spectra during the voltammetric sweep enables the adsorbed CO IR spectra to be monitored at electrode potentials where alcohol electrooxidation occurs. As pointed out above, two other SPAIRS methods were applied in this work. The classic one consisted in acquiring spectra at 50-mV intervals at 1 mV $s^{-1}$ and in a potential domain. The second technique was coupling chronoamperometry measurements with FTIRS acquisition at a fixed electrode potential (0.60 V and 0.70 V *vs* RHE for ethanol and glycerol, respectively) for 3 min. Regardless of the applied method and for each spectrum, a set of 528 interferograms were accumulated and treated by Fourier-transform. Two different working electrodes were used in this work: a vitreous carbon substrate (8-mm diameter) for GOR, and a gold substrate (disk with 7-mm diameter) for EOR and CO stripping experiments. To improve reflectivity at the electrode/solution interface, the catalytic ink composition was slightly modified by raising the volume of isopropanol (375 µL instead of 200 µL, as described above in section 2.4).
CO-stripping experiments in a 0.1 mol $L^{-1}$ NaOH solution were conducted with the same FTIRS data acquisition technique. Carbon monoxide was adsorbed at 0.2 V *vs* RHE for 5 min under potential control; then, the solution was deaerated with inert gas ($N_2$) for 20 min (to expel all free CO) before the cyclic voltammogram experiments.

## Acknowledgements

The authors thank the financial support from CAPES and CNPq. This study was partilly funded by Coordenação de Aperfeiçoamento de Pessoal de Nível Superior - Brasil (CAPES) - Finance Code 001. The collaborative program CAPES/COFECUB under grant n° 914/18 is gratefully acknowledged. The authors also acknowledge the financial support from the European Union (ERDF) and "Région Nouvelle-Aquitaine".

**Keywords:** palladium • rhodium • fuel cell • biomass valorizarion • alkaline medium

[1] N. Shaari, S. K. Kamarudin, R. Bahru, S. H. Osman, N. A. I. Md Ishak *Int J Energy Research*. **2021**, *45*, 6644-6688.
[2] Y. Holade, N. Tuleushova, S. Tingry, K. Servat, T. W. Napporn, H. Guesmi, D. Cornu, K. B. Kokoh *Catal Sci & Technol*. **2020**, *10*, 3071-3112.
[3] S. P. S. Badwal, S. Giddey, A. Kulkarni, J. Goel, S. Basu *Appl Energy*. **2015**, *145*, 80-103.
[4] Y. Wang, S. Zou, W.-B. Cai *Catalysts*. **2015**, *5*, 1507-1534.
[5] P. A. Cremonez, M. Feroldi, A. Feiden, J. Gustavo Teleken, D. José Gris, J. Dieter, E. de Rossi, J. Antonelli *Renew. Sustain. Energy Rev.* **2015**, *43*, 352-362.
[6] H. V. Amorim, M. L. Lopes, J. V. de Castro Oliveira, M. S. Buckeridge, G. H. Goldman *Appl Microbiol Biotechnol*. **2011**, *91*, 1267-1275.
[7] M. S. Ahmad, C. K. Cheng, S. Singh, H. R. Ong, H. Abdullah, C. S. Hong, G. K. Chua, M. R. Khan *J Nanosci Nanotechnol*. **2020**, *20*, 5916-5927.
[8] M. S. E. Houache, K. Hughes, R. Safari, G. A. Botton, E. A. Baranova *ACS Appl Mater. Interfaces*. **2020**, *12*, 15095-15107.
[9] Y. J. Duan, Z. L. Liu, B. Zhao, J. H. Liu *Inorg Chem Commun*. **2020**, *117*.
[10] L. Huang, J.-Y. Sun, S.-H. Cao, M. Zhan, Z.-R. Ni, H.-J. Sun, Z. Chen, Z.-Y. Zhou, E. G. Sorte, Y. J. Tong, S.-G. Sun *ACS Catal*. **2016**, *6*, 7686-7695.
[11] R. G. Da Silva, S. Aquino Neto, K. B. Kokoh, A. R. De Andrade *J. Power Sources*. **2017**, *351*, 174-182.
[12] R. S. Ferreira Jr, M. Janete Giz, G. A. Camara *J Electroanal Chem*. **2013**, *697*, 15-20.
[13] S. B. A. Hamid, N. Basiron, W. A. Yehye, P. Sudarsanam *Polyhedron*. **2016**, *120*, 124-133.
[14] Y. Holade, C. Morais, S. Arrii-Clacens, K. Servat, T. W. Napporn, K. B. Kokoh *Electrocatalysis*. **2013**, *4*, 167-187.
[15] Y. Kang, W. Wang, Y. Pu, J. Li, D. Chai, Z. Lei *Chem Eng J*. **2017**, *308*, 419-427.
[16] G. Dodekatos, S. Schünemann, H. Tüysüz *ACS Catal*. **2018**, *8*, 6301-6333.

[17] F. Zhu, K. Tu, L. Huang, X. Qu, J. Zhang, H. Liao, Z. Zhou, Y. Jiang, S. Sun *Electrochim. Acta*. **2018**, *292*, 208-216.
[18] M. Z. F. Kamarudin, S. K. Kamarudin, M. S. Masdar, W. R. W. Daud *Int. J. Hydrogen Energy*. **2013**, *38*, 9438-9453.
[19] E. H. Fontes, R. M. Piasentin, J. M. S. Ayoub, J. C. M. da Silva, M. H. M. T. Assumpção, E. V. Spinacé, A. O. Neto, R. F. B. de Souza *Mater. Renew. Sustain Energy*. **2015**, *4*, 1-10.
[20] S. Tang, G. Sun, J. Qi, S. Sun, J. Guo, Q. Xin, G. M. Haarberg *Chinese Journal of Catalysis*. **2010**, *31*, 12-17.
[21] J. Wang, H. Chen, Z. Hu, M. Yao, Y. Li *Catal. Rev.* **2015**, *57*, 79-144.
[22] A. Namdeo, S. M. Mahajani, A. K. Suresh *Journal of Molecular Catalysis A: Chemical*. **2016**, *421*, 45-56.
[23] H. Xu, P. Song, C. Fernandez, J. Wang, M. Zhu, Y. Shiraishi, Y. Du *ACS Applied Materials & Interfaces*. **2018**, *10*, 12659-12665.
[24] T. Hu, Y. Wang, Q. Liu, L. Zhang, H. Wang, T. Tang, W. Chen, M. Zhao, J. Jia *Int. J. Hydrogen Energy*. **2017**, *42*, 25951-25959.
[25] K. Jiang, P. Wang, S. Guo, X. Zhang, X. Shen, G. Lu, D. Su, X. Huang *Angew. Chem. Int. Ed.* **2016**, *55*, 9030-9035.
[26] H. Mao, L. Wang, P. Zhu, Q. Xu, Q. Li *Int. J. Hydrogen Energy*. **2014**, *39*, 17583-17588.
[27] C. Zhu, S. Guo, S. Dong *Adv. Mater.* **2012**, *24*, 2326-2331.
[28] L. A. Soares, C. Morais, T. W. Napporn, K. B. Kokoh, P. Olivi *J. Power Sources*. **2016**, *315*, 47-55.
[29] Q. Chang, Y. Hong, H. J. Lee, J. H. Lee, D. Ologunagba, Z. Liang, J. Kim, M. J. Kim, J. W. Hong, L. Song, S. Kattel, Z. Chen, J. G. Chen, S.-I. Choi *Proceedings of the National Academy of Sciences - PNAS*. **2022**, *119*, e2112109119-e2112109119.
[30] J. Bai, X. Xiao, Y.-Y. Xue, J.-X. Jiang, J.-H. Zeng, X.-F. Li, Y. Chen *ACS Applied Materials & Interfaces*. **2018**, *10*, 19755-19763.
[31] A. Maksić, M. Smiljanić, Š. Miljanić, Z. Rakočević, S. Štrbac *Electrochimica Acta*. **2016**, *209*, 323-331.
[32] T. F. Messa Moreira, S. A. Neto, C. Lemoine, K. B. Kokoh, C. Morais, T. W. Napporn, P. Olivi *RSC Advances*. **2020**, *10*, 35310-35317.
[33] P. Mukherjee, P. S. Roy, S. K. Bhattacharya *Int. J. Hydrogen Energy*. **2015**, *40*, 13357-13367.
[34] M. Li, W. P. Zhou, N. S. Marinkovic, K. Sasaki, R. R. Adzic *Electrochimica Acta*. **2013**, *104*, 454-461.
[35] K. Bergamaski, E. R. Gonzalez, F. C. Nart *Electrochim. Acta*. **2008**, *53*, 4396-4406.
[36] Y. Zhou, Y. Shen, J. Piao *ChemElectroChem*. **2018**, *5*, 1636-1643.
[37] C. R. Zanata, P. S. Fernández, H. E. Troiani, A. L. Soldati, R. Landers, G. A. Camara, A. E. Carvalho, C. A. Martins *Applied catalysis. B, Environmental*. **2016**, *181*, 445-455.
[38] E. H. Fontes, C. E. D. Ramos, J. Nandenha, R. M. Piasentin, A. O. Neto, R. Landers *Int J Hydrogen Energy*. **2019**, *44*, 937-951.
[39] E. Antolini *Appl. Catal. B: Environ.* **2009**, *88*, 1-24.
[40] B. Li, W. Su, X. Wang, X. Wang *Int. J. Hydrogen Energy*. **2016**, *41*, 14732-14746.
[41] Y. Holade, K. Servat, T. W. Napporn, K. B. Kokoh *Electrochim. Acta*. **2015**, *162*, 205-214.
[42] Y. Holade, R. G. da Silva, K. Servat, T. W. Napporn, C. Canaff, A. R. de Andrade, K. B. Kokoh *J. Mater. Chem. A*. **2016**, *4*, 8337-8349.
[43] J.-H. Choi, K.-W. Park, I.-S. Park, W.-H. Nam, Y.-E. Sung *Electrochimica Acta*. **2004**, *50*, 787-790.
[44] M. Harada, H. Einaga *J Colloid and Interface Sci*. **2007**, *308*, 568-572.
[45] M. M. S. Pupo, F. E. López-Suárez, A. Bueno-López, C. T. Meneses, K. I. B. Eguiluz, G. R. Salazar-Banda *J. Appl. Electrochem.* **2015**, *45*, 139-150.
[46] Y. Holade, N. Sahin, K. Servat, T. Napporn, K. Kokoh *Catalysts*. **2015**, *5*, 310-348.
[47] Y. Holade, C. Morais, K. Servat, T. W. Napporn, K. B. Kokoh *ACS Catal*. **2013**, *3*, 2403-2411.
[48] N. Ghanbari, S. J. Hoseini, M. Bahrami *Ultrasonics Sonochemistry*. **2017**, *39*, 467-477.
[49] M. A. F. Akhairi, S. K. Kamarudin *Int. J. Hydrogen Energy*. **2016**, *41*, 4214-4228.
[50] J. W. Arblaster *Platinum Metals Review*. **2012**, *56*, 181-189.
[51] T. Lopes, E. Antolini, F. Colmati, E. R. Gonzalez *J. Power Sources*. **2007**, *164*, 111-114.
[52] P. Wang, Y. Wen, S. Yin, N. Wang *Int. J. Hydrogen Energy*. **2017**, *42*, 24689-24696.
[53] R. Gómez, A. Rodes, J. M. Pérez, J. M. Feliu, A. Aldaz *Surf. Sci.* **1995**, *327*, 202-215.
[54] F. C. Nart, T. Iwasita *Electrochim. Acta*. **1996**, *41*, 631-636.
[55] E. R. Savinova, F. Hahn, N. Alonso-Vante *Phys. Chem. Chem. Phys.* **2007**, *9*, 5693-5699.
[56] L. Hu, G. Xia, L. Qu, C. Li, Q. Xin, D. Li *Journal of Molecular Catalysis A: Chemical*. **2001**, *171*, 169-179.
[57] S. Beyhan, J.-M. Léger, F. Kadırgan *Applied Catalysis B: Environmental*. **2014**, *144*, 66-74.
[58] D. K. Lambert *Electrochim. Acta*. **1996**, *41*, 623-630.
[59] P. Tonda-Mikiela, T. W. Napporn, C. Morais, K. Servat, A. Chen, K. B. Kokoh *Journal of the Electrochemical Society*. **2012**, *159*, H828-H833.
[60] L. C. Silva-Junior, G. Maia, R. R. Passos, E. A. de Souza, G. A. Camara, M. J. Giz *Electrochim. Acta*. **2013**, *112*, 612-619.
[61] J. P. I. De Souza, S. L. Queiroz, K. Bergamaski, E. R. Gonzalez, F. C. Nart *Journal of Physical Chemistry B*. **2002**, *106*, 9825-9830.
[62] L. Rao, Y.-X. Jiang, B.-W. Zhang, Y.-R. Cai, S.-G. Sun *Phys. Chem. Chem. Phys.* **2014**, *16*, 13662-13671.
[63] E. Higuchi, T. Takase, M. Chiku, H. Inoue *J. Power Sources*. **2014**, *263*, 280-287.
[64] P. Wnuk, A. Lewera *Electrochimica Acta*. **2020**, *330*, 12.
[65] M. Li, A. Kowal, K. Sasaki, N. Marinkovic, D. Su, E. Korach, P. Liu, R. R. Adzic *Electrochim. Acta*. **2010**, *55*, 4331-4338.
[66] A. Kowal, M. Li, M. Shao, K. Sasaki, M. B. Vukmirovic, J. Zhang, N. S. Marinkovic, P. Liu, A. I. Frenkel, R. R. Adzic *Nat. Mater.* **2009**, *8*, 325-330.
[67] G. M. Alvarenga, I. B. Coutinho Gallo, H. M. Villullas *J. Catal.* **2017**, *348*, 1-8.
[68] A. C. Garcia, M. J. Kolb, C. van Nierop y Sanchez, J. Vos, Y. Y. Birdja, Y. Kwon, G. Tremiliosi-Filho, M. T. M. Koper *ACS Catalysis*. **2016**, *6*, 4491-4500.
[69] L. W. H. Leung, M. J. Weaver *Langmuir*. **1990**, *6*, 323-333.

**Entry for the Table of Contents**

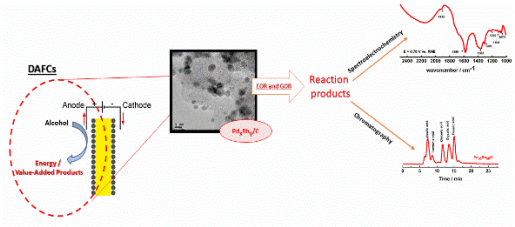


**Electronic effect within PdxRhy/C nanomaterials during EOR and GOR:** Rh as co-catalyst shifts the fuel oxidation towards lower potentials. On $Pd_{50}Rh_{50}$/C catalyst, the beneficial ligand effect helps to deplete the poisoning CO species strongly adsorbed on the catalyst surface. The identification of the reaction products by spectroelectrochemistry and chromatographic analyses demonstrated the ethanol C-C bond cleavage on EOR. Similarly, for GOR, the C-C bond cleavage products (oxalate, glycolate, formate, and carbonate) were identified.